

CHEMISTRY

Polymeric peptide pigments with sequence-encoded properties

Ayala Lampel,¹ Scott A. McPhee,¹ Hang-Ah Park,² Gary G. Scott,³ Sunita Humagain,^{4,5} Doeke R. Hekstra,⁶ Barney Yoo,⁷ Pim W. J. M. Frederix,⁸ Tai-De Li,¹ Rinat R. Abzalimov,¹ Steven G. Greenbaum,^{4,5} Tell Tuttle,³ Chunhua Hu,⁹ Christopher J. Bettinger,^{2,10,11} Rein V. Ulijn^{1,5,7*}

Melanins are a family of heterogeneous polymeric pigments that provide ultraviolet (UV) light protection, structural support, coloration, and free radical scavenging. Formed by oxidative oligomerization of catecholic small molecules, the physical properties of melanins are influenced by covalent and noncovalent disorder. We report the use of tyrosine-containing tripeptides as tunable precursors for polymeric pigments. In these structures, phenols are presented in a (supra)-molecular context dictated by the positions of the amino acids in the peptide sequence. Oxidative polymerization can be tuned in a sequence-dependent manner, resulting in peptide sequence-encoded properties such as UV absorbance, morphology, coloration, and electrochemical properties over a considerable range. Short peptides have low barriers to application and can be easily scaled, suggesting near-term applications in cosmetics and biomedicine.

Melanin pigments are found in most life forms, including plants, bacteria, fungi, and animals, and they have cardinal roles in organisms' coloration and protection from various (mainly photo- or free radical-induced) cell damage-causing stresses (1). In addition to their protective roles, melanin pigments exhibit dynamic coloration and optoelectronic properties, inspiring efforts to design energy storage devices (2), environmental sensors (3), surface-adherent coatings (4, 5), and colored films (6). The self-assembly and polymerization of natural melanin is regulated through complex pathways that include catalysis, templating, assembly, and oxidation under confinement, in a process that is not fully understood (1). Laboratory-based strategies to synthesize melanin-based analogs are challenging to apply and difficult to control. Heterogeneous

products typically consist of insoluble polymers with poorly defined chemical and structural compositions (7), thereby limiting the technological utility of this class of materials.

We reasoned that supramolecular materials (8, 9) formed by peptide building blocks (10–12) may offer promise for the formation of synthetic melanin-like materials (or polymeric pigments) because of the ability to precisely control the presentation of chemical functionality, and consequently reactivity, through noncovalent interactions. Even very short peptides, consisting of only two or three amino acids (13–16), have been shown to self-assemble to form discrete nanoscale materials (17). Furthermore, combining supramolecular self-assembly with catalytic [enzymatic (18, 19) or chemical (20, 21)] transformations provides spatiotemporal control (22) over the assembly process, giving rise to materials with kinetically tunable properties. Thus, combining catalysis and self-assembly offers an attractive approach for aqueous materials processing (22, 23).

Our first objective was to identify a small subset of peptides that self-assemble into supramolecular nanostructures with sequence-dependent properties. We focused on tripeptides containing tyrosine (Y) combined with the aggregation-prone aromatic amino acid phenylalanine (F) (14, 15) and a charged amino acid, aspartic acid (D) (Fig. 1A). To increase self-assembly propensity at neutral pH conditions, C-terminal amides were used. All six possible tripeptide combinations were studied, with those that contain paired aromatics expected to favor assembly (14, 15). After annealing by temporary heating (to 75°C) and subsequent cooling to room temperature, the six peptides exhibited distinctive macroscopic appearances (Fig. 1B, upper panel). The peptides with paired aromatics gave rise to self-assembly, whereas FDY and YDF remained clear solutions. YFD formed an opaque gel, FYD formed a suspension composed of amor-

phous aggregates, DFY formed a translucent gel, and DYF formed macroscopically observed needle-like crystalline fibers, eventually giving rise to a self-supporting gel (fig. S1 and movies S1 and S2).

We sought to leverage the variable peptide assemblies to control formation of polymeric pigments initiated by enzymatic oxidation of tyrosine residues. We used tyrosinase from *Agaricus bisporus*, which typically oxidizes tyrosine into 3,4-dihydroxyphenylalanine (DOPA) and further oxidation products, including DOPA-quinone, DOPAchrome, and dihydroxyindole, eventually forming polymers from these reactive species (fig. S2). Tyrosinase, which was previously shown to act on self-assembled peptides (24), was added directly to the tripeptide assemblies (after annealing). A readily observable, variable color change emerged for all tripeptides after 4 hours of incubation, with colors intensifying further over 24 hours, resulting in light brown coloration of the transparent solutions of FDY and YDF, beige coloration of the milky FYD suspension, and brown-black colors for YFD, DYF, and DFY, suggesting that the oxidized peptides polymerized to different extents (Fig. 1B, lower panel). As a control, we used tyrosine, which rapidly oxidized and polymerized, as observed by the black color of the sample and the polymeric precipitate.

Nanoscale morphologies were determined by transmission electron microscopy (TEM) (Fig. 2A) and atomic force microscopy, which showed that the nanostructures' stiffness depended on peptide sequence (fig. S3). YFD and DFY assembled into a dense network of nanofibrils, whereas needle-like crystalline fibers were seen in DYF (fig. S4), with amorphous aggregates observed for the others. To assess supramolecular order, the crystallization of DFY provided a convenient starting point. Single-crystal x-ray diffraction (XRD) (table S1) revealed five main interfaces that stabilize the crystal lattice (Fig. 2B). Along the *x* axis, the peptides formed parallel β -sheets that extended laterally by two interfaces along the *y* direction: (i) hydrogen bonding between the amide groups (Fig. 2B, "1") and (ii) salt bridges of the aspartate carboxylate groups and terminal amines ("2"). Along the *z* axis, the β -sheets were packed through hydrogen bonding of the tyrosine hydroxyl groups ("3") and aromatic stacking ("4") into a three-dimensional (3D) lattice. Single crystals could also be obtained by slow cooling of the YFD solution. XRD showed similar interactions to those in DFY, but with different consequences: For YFD, a single backbone-backbone hydrogen bond was observed between molecules (Fig. 2C, "2"). The columns interacted laterally by aromatic stacking ("1"), yielding 2D planes of aromatically stacked groups, and by alternating hydrogen-bonding networks coupling the aspartate-amine salt bridges ("3"), C-terminal amides, and tyrosine hydroxyl groups through well-ordered water molecules ("4"). The consequence of the observed packing was a substantially different orientation of the paired aromatics (figs. S5 to S8)—in opposite (anti) or same (syn) orientations for DYF and YFD with respect to the peptide backbone.

¹Advanced Science Research Center at the Graduate Center of the City University of New York, 85 Saint Nicholas Terrace, New York, NY 10031, USA. ²Department of Materials Science and Engineering, Carnegie Mellon University, 5000 Forbes Avenue, Pittsburgh, PA 15213, USA. ³WestCHEM and Department of Pure and Applied Chemistry, University of Strathclyde, 295 Cathedral Street, Glasgow G1 1XL, UK.

⁴Department of Physics and Astronomy, Hunter College, City University of New York, 695 Park Avenue, New York, NY 10065, USA. ⁵Ph.D. programs in Biochemistry, Chemistry and Physics, The Graduate Center of the City University of New York, NY 10016, USA. ⁶Department of Molecular and Cellular Biology, School of Engineering and Applied Sciences, FAS Center for Systems Biology, Harvard University, Cambridge, MA 02138, USA. ⁷Department of Chemistry, Hunter College, City University of New York, 695 Park Avenue, New York, NY 10065, USA. ⁸Groningen Biomolecular Sciences and Biotechnology Institute, Rijksuniversiteit Groningen, Groningen, Netherlands. ⁹Department of Chemistry, Silver Center for Arts and Science, 100 Washington Square East, New York University, New York, NY 10003, USA. ¹⁰Department of Biomedical Engineering, Carnegie Mellon University, 5000 Forbes Avenue, Pittsburgh, PA 15213, USA. ¹¹McGowan Institute of Regenerative Medicine, 450 Technology Drive, Suite 300, Pittsburgh, PA 15219, USA.

*Corresponding author. Email: rein.ulijn@asrc.cuny.edu

To shed more light on the organization of the tripeptides, including those for which crystal structures could not be obtained under the assembly conditions, we used Fourier transform infrared spectroscopy (FTIR) (Fig. 2D). FDY, YDF, and FYD did not show evidence of periodically organized intermolecular interactions, as indicated by broad bands at 1652 cm^{-1} (internal amide) and 1672 cm^{-1} (terminal amide) in the FTIR spectrum, which is in agreement with disorder observed by TEM. For the assembled DFY and DYF peptides, these bands redshifted to 1620 to 1640 cm^{-1} and 1658 cm^{-1} , respectively, which suggests a β -sheet-like organization. The YFD spectrum implies a different packing geometry, with additional narrow, redshifted bands in the amide region, but an additional shift of the aspartate carboxylate band from 1580 cm^{-1} to 1560 cm^{-1} ; this suggests intramolecular salt bridge formation with the amine group of the N terminus, in agreement with the crystal structure (Fig. 2C), which helps to stabilize paired aromatics in the syn configuration.

The six peptides showed variable crystallinity (figs. S9 to S14). FYD, YFD, and DYF formed highly crystalline materials, and DFY exhibited lower crystallinity, evidenced by the peak intensity and broadness. In contrast, FDY and YDF formed amorphous materials. However, all the peptides shared some common features in terms of molecular stacking, reflected by the peaks in the ranges of 4.4 to 4.8 \AA and 2.9 to 3.2 \AA . In addition, the diffraction patterns of DFY and DYF were similar, indicating the structural resemblance of these two peptides.

To examine the relative stability of the different conformations of the monomers, molecular dynamics simulations were carried out (25, 26) (Fig. 2, E and F). The results demonstrate that the six peptides have different preferential conformations, which is reflected both in the assembled state and in solution, depending in a pairwise manner on the position of the aspartic acid. The following relationships exist: Tyrosine and phenylalanine residues are presented in anti (DXX) or syn (XXD) configuration, which is in agreement with the crystal structures obtained. When the aspartic acid is in the central position (XDX), the preferred conformations have dihedral angles of $\sim 90^\circ$, which limits the potential for extended stacking.

We subsequently investigated whether the pairwise sequence-dependent supramolecular order of the peptides influences enzymatic oxidation and further polymerization pathways. Wide-angle x-ray scattering (WAXS) and solid-phase FTIR data showed loss of order, with the strongest effect observed for oxidized DXX (DXX_{ox}) and less for oxidized XXD (XXD_{ox}), whereas oxidized XDX (XDX_{ox}) remained disordered (Fig. 3, A to C). The peptides lost supramolecular order (Fig. 3, A and B, and figs. S9 to S14), retaining few structural features corresponding to the molecular packing, according to the peaks at about 4.5 and 2.9 \AA . The FTIR spectra (Fig. 3C) showed narrow, redshifted absorptions of the amide group in FYD, YFD, DFY, and DYF that disappeared following oxidation in favor of broad absorptions at 1650 to 1675 cm^{-1} . Additionally, tyrosine-specific ring modes were lost

(e.g., 1516 cm^{-1}), and a new band absorption assigned to quinone was observed around 1680 cm^{-1} , confirming catechol oxidation.

High-performance liquid chromatography (HPLC) analysis showed (near-)complete conversions of peptides to oxidation products for both the disordered (XDX_{ox}) and highly ordered (DXX_{ox}) peptides, with lower conversions observed for XXD_{ox} (FYD_{ox} giving lower conversion than YFD_{ox}) (table S2). Under the conditions examined, peptide assembly had a more pronounced effect on oxidation and polymerization than did the position of the tyrosine within the tripeptides. Early-stage conversions were higher for XDX_{ox} peptides than for the assembling counterparts (fig. S15). However, early-stage kinetics were similar for the non-assembling FDY_{ox} and YDF_{ox}. We conclude that the overall polymerization process is dictated more by the supramolecular order of the precursors and less by enzyme affinity.

Liquid chromatography-mass spectrometry (LC-MS) data obtained after 24 hours of oxidation revealed the expected catechol and quinone, as well as a wide range of dimeric and trimeric species with different connections (Fig. 3, D to F, and table S3). A pairwise relationship is again clear from these data, with XDX_{ox} peptides giving rise to complete conversion of the precursors to oligomers and polymers, XXD_{ox} giving medium conversion with intermediate polymerization, and DXX_{ox} peptides giving rise to formation of extensive oligomeric and polymeric species (table S3 and Fig. 3D). In each case, the ultraviolet (UV) absorbance of the polymeric species was substantially redshifted from precursors, as would be expected for an extensive catechol-quinone network.

The polymers had distinct morphologies as observed by optical microscopy (Fig. 4A). Although YFD_{ox} maintained a 1D morphology, it formed much larger fibers, suggesting a degree of lateral aggregation that may be facilitated by the positioning of 2D sheets of reactive aromatic species at interfaces, as seen in the crystal structure (Fig. 2C). DFY_{ox} polymerized into extended 2D sheets, whereas DYF_{ox} formed spheres. These morphologies, and the amorphous structures of the other oxidized peptides, were also observed by TEM (fig. S16). Whereas the DFY_{ox} sheets and YFD_{ox} fibers were in the solid phase, the DYF_{ox} spheres remained dispersed in the aqueous buffer.

The greatest contrast among structures was evident in DXX_{ox} tripeptides, which, starting from similar molecular packing of the precursors, showed high levels of polymerization accompanied by loss of order. For these peptides, a subtle difference in sequence dictated the initial (crystalline fibers versus supramolecular fibers) and oxidized (spheres versus sheets) morphologies. For DFY_{ox}, we propose that the anti conformation of aromatic side chains is favorable for polymerization along the length of the β -sheet but also laterally between neighboring fibrils, eventually resulting in loss of supramolecular structures (fibrils) and formation of extended, micron-scale 2D sheets. Time-course TEM analysis of DFY (fig. S17) supports this mechanism for the fiber-to-sheet transition,

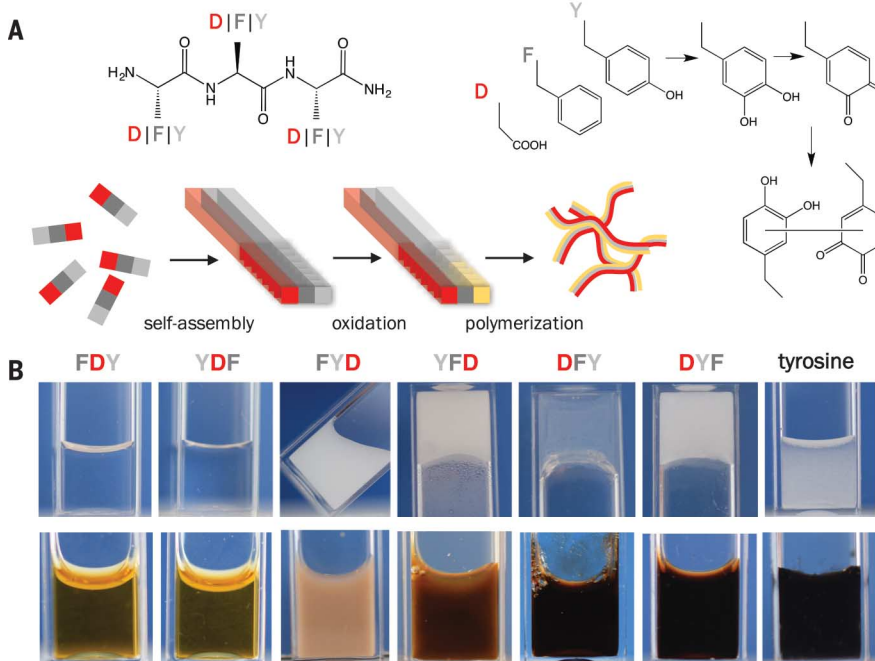


Fig. 1. Sequence-dependent polymeric peptide pigments. (A) Schematic representation of the selected tripeptide sequences and the controlled formation of polymeric peptide pigments by enzymatic oxidation and further polymerization of preorganized tripeptides. (B) Macroscopic images of the materials formed by the self-assembly of the tripeptides (20 mM in phosphate buffer at pH 8), before (top) and after (bottom) 24 hours of enzymatic oxidation (0.2 $\mu\text{g}/\mu\text{l}$), including oxidation of tyrosine as a control.

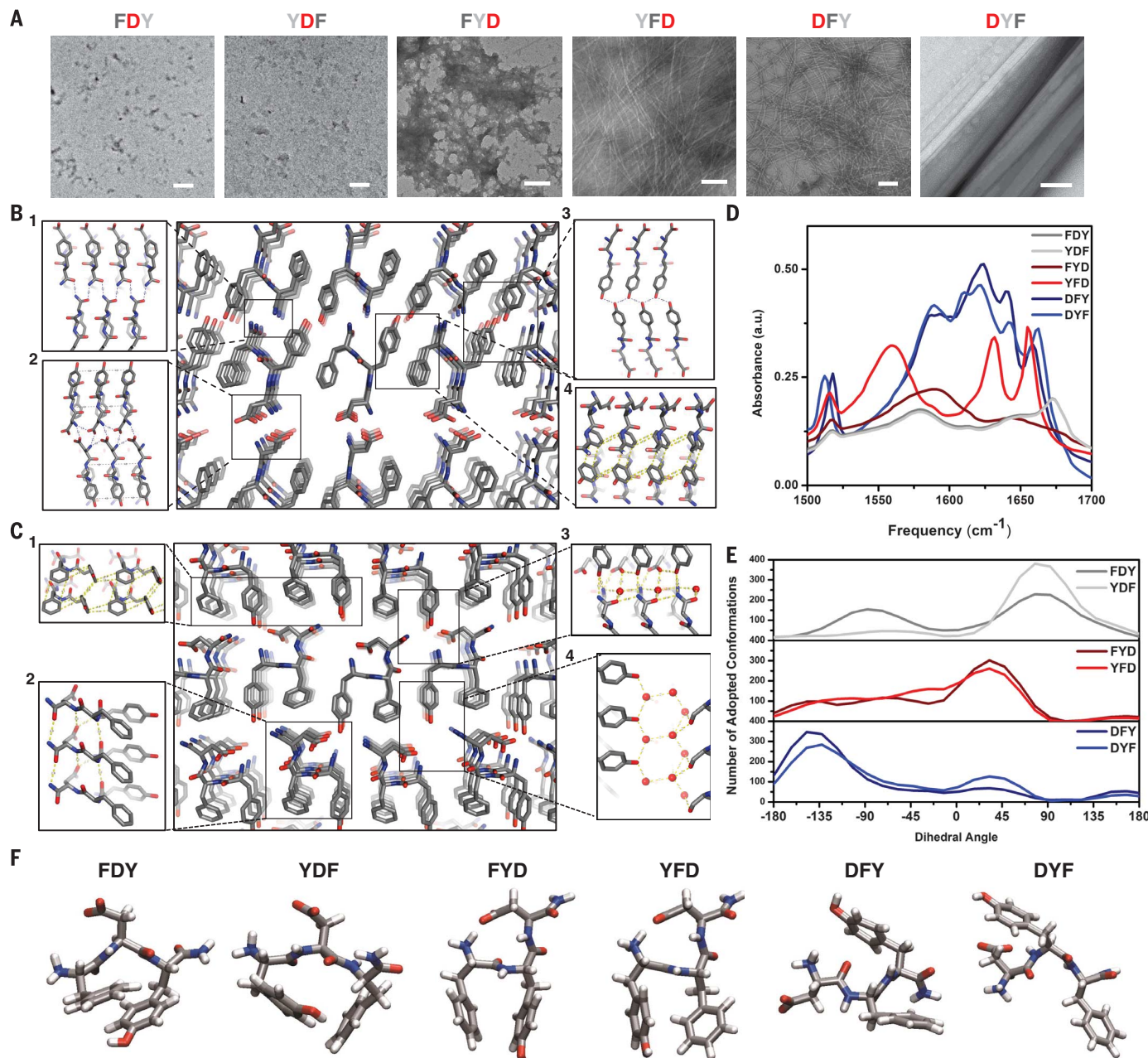


Fig. 2. Differential organization in tripeptide assemblies. (A) TEM micrographs of structures formed by self-assembly of tripeptides. Scale bars, 100 nm. (B and C) DYF (B) and YFD (C) crystal structures, showing different interfaces forming the lattice. (D) FTIR absorption spectra of the tripeptides (20 mM in D_2O phosphate buffer at pH 8). a.u., arbitrary units. (E) Distribution of the CZ(Y)-CA(Y)-CA(F)-CZ(F) dihedral angle for each peptide over the course of 50 ns. (F) Preferred conformations for each peptide.

revealing the formation of dark layers on the fibrils' surface (4 hours); these layers further assembled and polymerized into 2D sheets that extended from the fiber surface (1 week). For DYF, a different orientation of tyrosine gave rise to an additional stabilizing interaction (Y-Y) within the crystal lattice (27) (Fig. 2B). Oxidation of tyrosine eliminated hydrogen bonding in these residues, thereby disrupting the crystalline fiber and reconfiguring the peptides into spherical assemblies. These data are in agreement with the loss of the original packing and

subsequent polymerization observed for both DFY_{ox} and DYF_{ox} by FTIR, WAXS, and LC-MS (Fig. 3).

The results show that supramolecular order in peptide precursors can be systematically converted into disordered polymeric pigments, resulting in variable characteristics that relate to their functionality (Fig. 4). UV-visible (UV-Vis) measurements showed different broadband spectra, with DFY_{ox} showing absorption throughout the visible region (420 to 650 nm) and high absorption observed for FYD_{ox} possibly contributed by

highly scattering aggregates (Fig. 4B). The observed maximum around 340 nm for YFD_{ox} , together with the LC-MS (Fig. 3, D and E) and HPLC analyses (fig. S15D), suggest that the N-terminal positioning of the catechol results in a lower degree of connectivity and cross-linking.

Oxidized peptides were configured into cathodes in aqueous half-cell configurations. The charge storage capacity can provide an estimate of the concentration of redox-active components, and the shape of the discharge curve can provide insight into the distribution of morphological

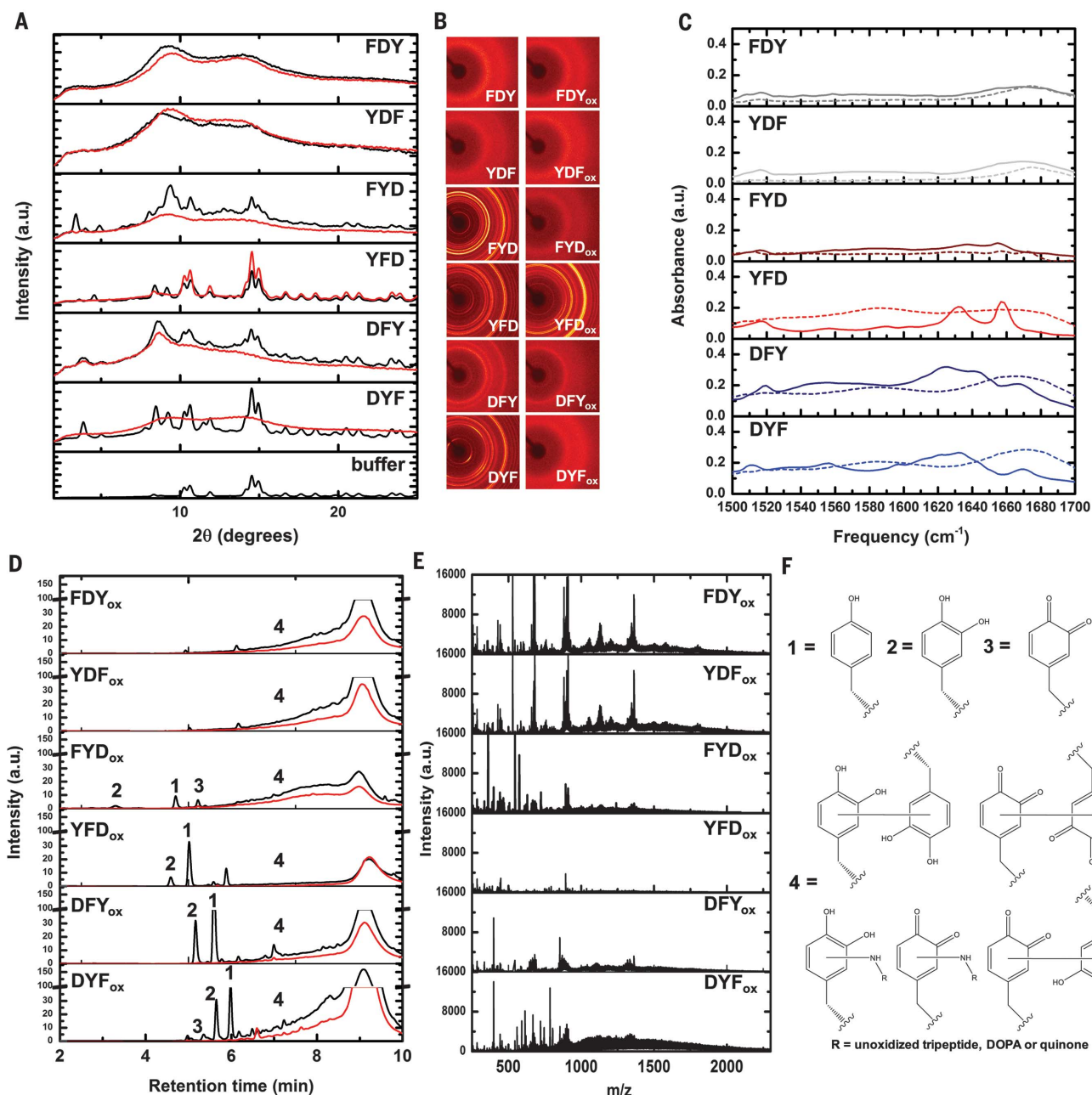


Fig. 3. From order to disorder in polymeric peptide pigments. (A and B) WAXS analysis including 1D (A) and 2D (B) patterns of tripeptides before [black in (A)] or after [red in (A)] 24 hours of enzymatic oxidation. θ, angle. (C) FTIR absorption spectra of tripeptides before (solid lines) or after (dashed lines) 24 hours of enzymatic oxidation. (D) LC-MS chromatograms at 280 nm (black) and 350 nm (red) of the soluble fraction of tripeptides oxidized for 24 hours. Numbers refer to (F).

(E) Summed mass/charge (*m/z*) intensities of soluble higher-molecular-weight polymers composed of heterogeneously connected monomers ["4" in (F)] eluted between 8 and 10 min. (F) Chemical structures of the nonoxidized peptides ("1") and the oxidation products 3,4-dihydroxyphenylalanine ("2") and 3,4-quinone ("3") in the context of tripeptides. "4," connectivity of potential aryl cross-linked and Michael addition products (supplementary materials).

phases. For this purpose, electrodes were fabricated by compacting peptide melanin powders into a stainless steel support mesh (Fig. 4C) (28). For all systems tested, the potentials became monotonically more negative during discharge, which confirms that these materials are largely disordered. DFY_{ox} 2D sheets exhibited the highest specific charge storage capacity, followed by DYF_{ox} (Fig. 4, D and E), which is attributed to an increase in the

concentration of redox-active tyrosine-based derivatives (2, 29) and is confirmed by cyclic voltammetry (CV) (fig. S18). Capacitive storage is the likely source of differential capacities in cathodes composed of YFD_{ox} versus FYD_{ox}, which are otherwise largely devoid of redox behavior as assessed by CV. The specific capacity of DFY_{ox} is comparable to that measured in natural eumelanin cathodes and less than that of the syn-

thetic melanin-based cathodes (fig. S19). CV of DFY_{ox}-based cathodes showed multiple redox peaks that are not commonly observed in other types of natural and synthetic melanin-based pigments (30), which are attributed to the presence of multiple types of polyphenols with a variety of redox behaviors. Electron paramagnetic resonance (EPR) suggests that DFY_{ox} sheets exhibit the highest gravimetric concentration of radical content

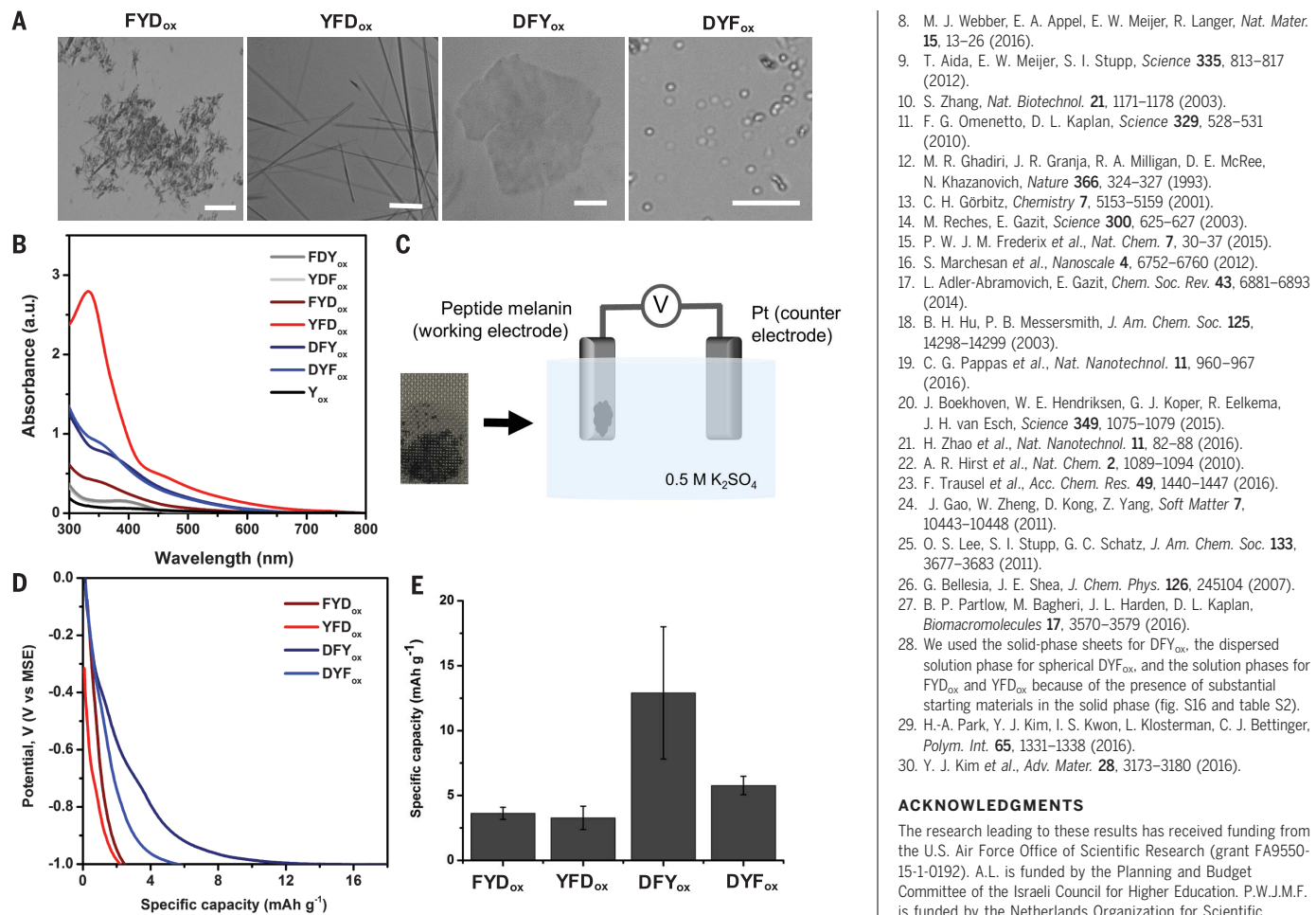


Fig. 4. Morphology, UV-Vis absorption, and electrochemical properties of polymeric peptide pigments. (A) Structures formed by the polymeric peptide pigments at the micron scale, observed using optical microscopy. Scale bars for FYD_{ox}, YFD_{ox}, and DFY_{ox}, 20 μm ; for DYF_{ox}, 10 μm . (B) UV-Vis absorption spectra of solution fractions of polymeric peptide pigments and oxidized tyrosine. (C) Macroscopic image of polymeric peptide pigment electrode and schematic illustration of the electrochemical cell used for discharge measurements. (D) Electrochemical potential profiles and (E) average specific capacity of polymeric peptide pigments. Error bars, standard errors ($n = 3$). MSE, mercury/mercurous sulfate electrode; Ah, ampere hour.

among the polymeric peptide pigments (fig. S20 and table S4). We propose that relatively higher semiquinone concentrations correspond to not only higher overall concentrations of catechols, but also molecular configurations that permit comproportionation reactions. The attenuated EPR signal observed in the polymeric peptide pigments is consistent with this model, owing to the smaller overall catechol concentrations and reduced catechol-catechol interactions compared with natural eumelanins.

We demonstrate the ability to leverage differential assembly and reactivity to achieve tunable polymeric pigments and find that supramolecular order in precursors is inversely correlated to disorder in resulting polymers. This gives rise to control and tunability over the properties of the materials. The possibility of marrying the diverse structures that can be accessed in short-peptide

assemblies with melanin-like properties facilitates fundamental studies related to how tunable functions are dictated by order, as well as by disorder. Moreover, because short peptides have low barriers to application and can be easily scaled, they may have near-term applications in cosmetics and biomedicine.

REFERENCES AND NOTES

1. P. Meredith, T. Sarna, *Pigment Cell Res.* **19**, 572–594 (2006).
2. Y. J. Kim, W. Wu, S. E. Chun, J. F. Whitacre, C. J. Bettinger, *Proc. Natl. Acad. Sci. U.S.A.* **110**, 20912–20917 (2013).
3. C. Shillingford, C. W. Russell, I. B. Burgess, J. Aizenberg, *ACS Appl. Mater. Interfaces* **8**, 4314–4317 (2016).
4. H. Lee, S. M. Dellatore, W. M. Miller, P. B. Messersmith, *Science* **318**, 426–430 (2007).
5. G. Fichman et al., *ACS Nano* **8**, 7220–7228 (2014).
6. M. Xiao et al., *ACS Nano* **9**, 5454–5460 (2015).
7. M. d'Ischia, A. Napolitano, V. Ball, C. T. Chen, M. J. Buehler, *Acc. Chem. Res.* **47**, 3541–3550 (2014).
8. M. J. Webber, E. A. Appel, E. W. Meijer, R. Langer, *Nat. Mater.* **15**, 13–26 (2016).
9. T. Aida, E. W. Meijer, S. I. Stupp, *Science* **335**, 813–817 (2012).
10. S. Zhang, *Nat. Biotechnol.* **21**, 1171–1178 (2003).
11. F. G. Omenetto, D. L. Kaplan, *Science* **329**, 528–531 (2010).
12. M. R. Ghadiri, J. R. Granja, R. A. Milligan, D. E. McRee, N. Khazanovich, *Nature* **366**, 324–327 (1993).
13. C. H. Görbitz, *Chemistry* **7**, 5153–5159 (2001).
14. M. Reches, E. Gazit, *Science* **300**, 625–627 (2003).
15. P. W. J. M. Frederix et al., *Nat. Chem.* **7**, 30–37 (2015).
16. S. Marchesani et al., *Nanoscale* **4**, 6752–6760 (2012).
17. L. Adler-Abramovich, E. Gazit, *Chem. Soc. Rev.* **43**, 6881–6893 (2014).
18. B. H. Hu, P. B. Messersmith, *J. Am. Chem. Soc.* **125**, 14298–14299 (2003).
19. C. G. Pappas et al., *Nat. Nanotechnol.* **11**, 960–967 (2016).
20. J. Boekhoven, W. E. Hendriksen, G. J. Koper, R. Eelkema, J. H. van Esch, *Science* **349**, 1075–1079 (2015).
21. H. Zhao et al., *Nat. Nanotechnol.* **11**, 82–88 (2016).
22. A. R. Hirst et al., *Nat. Chem.* **2**, 1089–1094 (2010).
23. F. Trausel et al., *Acc. Chem. Res.* **49**, 1440–1447 (2016).
24. J. Gao, W. Zheng, D. Kong, Z. Yang, *Soft Matter* **7**, 10443–10448 (2011).
25. O. S. Lee, S. I. Stupp, G. C. Schatz, *J. Am. Chem. Soc.* **133**, 3677–3683 (2011).
26. G. Bellesia, J. E. Shea, *J. Chem. Phys.* **126**, 245104 (2007).
27. B. P. Partlow, M. Bagheri, J. L. Harden, D. L. Kaplan, *Biomacromolecules* **17**, 3570–3579 (2016).
28. We used the solid-phase sheets for DFY_{ox}, the dispersed solution phase for spherical DFY_{ox}, and the solution phases for FYD_{ox} and YFD_{ox} because of the presence of substantial starting materials in the solid phase (fig. S16 and table S2).
29. H.-A. Park, Y. J. Kim, I. S. Kwon, L. Klosterman, C. J. Bettinger, *Polym. Int.* **65**, 1331–1338 (2016).
30. Y. J. Kim et al., *Adv. Mater.* **28**, 3173–3180 (2016).

ACKNOWLEDGMENTS

The research leading to these results has received funding from the U.S. Air Force Office of Scientific Research (grant FA9550-15-1-0192). A.L. is funded by the Planning and Budget Committee of the Israeli Council for Higher Education. P.W.J.M.F. is funded by the Netherlands Organization for Scientific Research (Veni program, grant number 722.015.005). The authors are grateful for support from the Materials Research Science and Engineering Center program of the National Science Foundation (NSF) under award numbers DMR-02082041 and DMR-1420073 and for the assistance of C.-H. (J.) Chen at the University of Indiana and Y.-S. Chen at the ChemMatCARS Sector 15 of the Advanced Photon Source (APS), which is principally supported by the NSF (grant number CHE-1346572). Use of the APS, an Office of Science User Facility operated for the U.S. Department of Energy (DOE) Office of Science by Argonne National Laboratory, was supported by the U.S. DOE under contract no. DE-AC02-06CH11357. We thank A. Bykov (Department of Physics, City College of New York) for help with WAXS analysis and J. Gu and V. M. Menon (Department of Physics, City College of New York) for help with UV-Vis analysis. Hunter Mass Spectrometry is supported by the City University of New York, the NSF, and the National Institute on Minority Health and Health Disparities (NIMHD) of the NIH. Results were obtained using the Engineering and Physical Sciences Research Council-funded ARCHIE-WeSt High Performance Computer (www.archie-west.ac.uk; grant number EP/K000586/1). The City University of New York has filed a provisional patent application (serial number 62/385,544) for technology related to this work.

SUPPLEMENTARY MATERIALS

www.sciencemag.org/content/356/6342/1064/suppl/DC1

Materials and Methods

Figs. S1 to S20

Tables S1 to S4

References (31, 32)

Movies S1 and S2

Data S1

29 November 2016; accepted 8 May 2017
10.1126/science.aal5005